Injection Process of Pickup Ion Acceleration at an Oblique Heliospheric Termination Shock

Matsukiyo, Shuichi
Faculty of Engineering Sciences, Kyushu University

Matsumoto, Yosuke
Institute for Advanced Academic Research, Chiba University

出版情報：The Astrophysical Journal Letters. 970 (2), pp.L37-, 2024-07-29. American Astronomical Society
バージョン：

The Astrophysical Journal Letters, 970:L37 (6pp), 2024 August 1 https://doi.org/10.3847/2041-8213/ad5d73

Injection Process of Pickup Ion Acceleration at an Oblique Heliospheric Termination Shock

Shuichi Matsukiyo[1,2,3] and Yosuke Matsumoto[4]
[1] Faculty of Engineering Sciences, Kyushu University, 6-1 Kasuga-Koen, Kasuga, Fukuoka 816-8580, Japan; matsukiy@esst.kyushu-u.ac.jp
[2] International Research Center for Space and Planetary Environmental Science (i-SPES), Kyushu University, Motooka, Nishi-Ku, Fukuoka 819-0395, Japan
[3] Institute of Laser Engineering, Osaka University, 2-6, Yamadaoka, Suita, Osaka 565-0871, Japan
[4] Institute for Advanced Academic Research, Chiba University, 1-33 Yayoi-cho, Inage-ku, Chiba 263-8522, Japan
Received 2024 May 26; revised 2024 June 29; accepted 2024 July 1; published 2024 July 29

Abstract

The injection process of pickup ion acceleration at a heliospheric termination shock is investigated. Using two-dimensional fully kinetic particle-in-cell simulation, accelerated pickup ions are self-consistently reproduced by tracking long time evolution of shocks with an unprecedentedly large system size in the shock normal direction. Reflected pickup ions drive upstream large-amplitude waves through resonant instabilities. Convection of the large-amplitude waves causes shock surface reformation and alters the downstream electromagnetic structure. A part of pickup ions are accelerated to tens of upstream flow energy in the timescale of $\sim$100 times inverse ion gyrofrequency. The initial acceleration occurs through the shock surfing acceleration (SSA) mechanism followed by the shock drift acceleration mechanism. Large electrostatic potential accompanied by the upstream waves enables the SSA to occur.

Unified Astronomy Thesaurus concepts: Heliosphere (711)

1. Introduction

A collisionless shock is ubiquitous in space. It is an energy converter formed in a supersonic plasma flow. Various explosive phenomena in space, as well as many stellar winds and astrophysical jets, are accompanied by collisionless shocks. One of the outstanding issues of collisionless shock physics is the mechanism of particle acceleration occurring around it. It is believed that cosmic rays are produced in a collisionless shock through the diffusive shock acceleration (DSA) mechanism (e.g., Blandford & Eichler 1987). In order for the DSA mechanism to work, preaccelerated nonthermal particles have to exist near a shock front. However, the mechanism producing such nonthermal particles, which should be dominated by complex microstructures of local electromagnetic fields, has been an open question for a long time. This is called the injection problem (Balogh & Treumann 2013; Burgess & Scholer 2015; Amano et al. 2022).

The heliospheric termination shock (HTS) is thought to be an ideal laboratory to study the injection process because the anomalous cosmic rays (ACRs), having typically several tens of megaelectron volts (MeV), are believed to be accelerated there (Chalov 2006). However, the Voyager spacecraft observed only a small amount of ACRs in the heliosheath, downstream of the HTS (e.g., Stone et al. 2005). The reason for this was inferred by McComas & Schwadron (2006) as being that efficient acceleration of ACRs occurs in the flank regions of the HTS, where the geometrical condition of the local HTS is more suitable for particle acceleration than that of the HTS where the two Voyager spacecraft crossed.

On the other hand, Giacalone et al. (2021) recently performed hybrid (kinetic ions with charge neutralizing electron fluid) simulations and showed that the acceleration rate of low-energy ($\lesssim$50 keV) pickup ions (PUIs) is more or less independent of the position in the HTS. The nonthermal particles in this energy range are expected to have their global map obtained in the near future through the Interstellar Mapping and Acceleration Probe (IMAP) mission. In their simulation (Giacalone et al. 2021), turbulence in the solar wind is taken into account. Particles are expected to undergo scattering by the turbulent field, leading to some degree of acceleration, and there is a potential for these particles to be injected into the DSA process (Giacalone et al. 2021; Pitňa et al. 2021; Trotta et al. 2021, 2022; Zank et al. 2021; Nakanotani et al. 2022; Wang et al. 2023). Another expected effect is the tilting of the local magnetic field line. In oblique shocks particles reflected by the shock travel upstream, exciting waves themselves and generating mildly accelerated particles injected into the DSA process. Such a situation may occur in some specific regions of termination shock and perhaps locally everywhere when solar wind is turbulent. In this scenario, the generation of mildly accelerated particles needs to occur near the shock, but the detailed mechanism is not well understood. This study aims to validate the latter scenario.

It is thought that initial acceleration sets in when a particle is reflected at the shock. In general, shock potential strongly affects the reflection of PUIs. In a hybrid simulation, the electrostatic potential is typically derived from a generalized Ohm's law, which includes a term proportional to the electron pressure gradient. Calculating this electron pressure gradient term requires assuming a specific equation of state for electrons. Consequently, the electrostatic field in a hybrid simulation becomes model dependent. Swisdak et al. (2023) pointed out that fully kinetic particle-in-cell (PIC) simulation leads to higher fluxes and maximal energies of PUIs than hybrid simulation, likely due to differences in the shock potential. Before the Voyager spacecraft crossed the HTS, the shock surfing acceleration (SSA) was widely accepted as a plausible mechanism of injection (Lee et al. 1996; Zank et al. 1996). However, Voyager did not observe the expected amount

of high-energy particles when they crossed the HTS (Decker et al. 2008). This implies that the SSA mechanism did not work effectively either. The reason that SSA does not work in the termination shock was explained by Matsukiyo & Scholer (2014). They conducted a one-dimensional fully kinetic PIC simulation of (quasi-)perpendicular shock and showed that most of potential jump in a PUI-mediated shock occurs in an extended foot produced by reflected PUIs so that the potential jump at a shock ramp is insufficiently small for the SSA mechanism to work. The shock potential in an oblique PUI-mediated shock has not been extensively studied so far.

Although the ab initio PIC simulation is useful to reproduce complex multiscale electromagnetic structures responsible for injection processes, it requires large numerical cost. That is why PIC simulation of a collisionless shock in a plasma containing PUIs has been limited mainly to the cases with one spatial dimension (e.g., Lee et al. 2005; Matsukiyo et al. 2007; Matsukiyo & Scholer 2011, 2014; Oka et al. 2011; Lembege & Yang 2016, 2018; Lembege et al. 2020). Two-dimensional PIC simulations including PUIs were first conducted by Yang et al. (2015). They focused on the impact of PUIs on shock front nonstationarity of a perpendicular shock, $\Theta_{Bn} = 90°$, and energy dissipation up to $t = 8\Omega_i^{-1}$, where Θ_{Bn} denotes the shock angle, the angle between shock normal and upstream magnetic field, and Ω_i is upstream ion cyclotron frequency. Kumar et al. (2018) performed longer simulation up to $t \sim 30\Omega_i^{-1}$ for quasi-perpendicular shocks, $\Theta_{Bn} = 80°$. They paid more attention to energy distribution of PUIs and solar wind ions (SWIs) for different upstream velocity distribution functions of PUIs. A little longer calculation up to $t \sim 40\Omega_i^{-1}$ was done with $\Theta_{Bn} = 70°$ by Swisdak et al. (2023). However, since the shock angle is close to or equal to perpendicular in the above previous studies, significant acceleration of PUIs is not reproduced. Indeed, when considering the average values, the shock angle of the termination shock is nearly perpendicular. However, as mentioned in the previous paragraph, it is easy to predict that the local shock angle fluctuates significantly owing to the effects of solar wind turbulence and unsteady solar activity. This fluctuation could have important implications for the ion injection process.

In this study we focus on the initial acceleration, which is often called the injection process, of PUIs at an oblique HTS. The microstructures of a local oblique HTS with $\Theta_{Bn} = 50°$, and with 60° and 70° for comparison, mediated by the presence of PUIs and their impact on PUI acceleration are discussed by performing two-dimensional full PIC simulation with unprecedentedly long simulation time ($t_{\max} = 125\Omega_i^{-1}$).

2. PIC Simulation

2.1. Settings

The system size in the x–y simulation domain is $L_x \times L_y = 2000 v_A/\Omega_i \times 40.96 v_A/\Omega_i$, which is divided by 200,000 × 4096 grid points. Here v_A denotes upstream Alfvén velocity. The so-called injection method is utilized to form a shock. An upstream homogeneous plasma consisting of solar wind electrons and ions, as well as PUIs, is continuously injected from the moving boundary at finite x, while the plasma and electromagnetic waves are reflected at the fixed rigid wall boundary at $x = 0$. The simulation frame is a downstream plasma frame, so that a shock propagates toward the positive x-direction. Initially 20 particles per cell are distributed for each species. The distribution functions of the injected solar wind electrons and ions are a shifted Maxwellian, and that of the injected PUIs is a shifted-shell distribution with zero width of the shell velocity. The injection (or drift) speed is $-3.75 v_A$, so that the Alfvén Mach number of the shock is $M_A \approx 5.5$ for $\Theta_{Bn} = 50°$, $M_A \approx 5.8$ for $\Theta_{Bn} = 60°$, and $M_A \approx 5.9$ for $\Theta_{Bn} = 70°$. Here the upstream magnetic field is in the x–y simulation plane. These values of the Mach number are close to the one estimated by Li et al. (2008) using Voyager 2 data, which is a little smaller than the value assumed in Giacalone et al. (2021). The upstream electron beta is $\beta_e = 0.25$, and the SWI temperature is the same as that of electrons, $T_i = T_e$. The beta value is slightly larger than the estimates by Li et al. (2008) and the values assumed by Giacalone et al. (2021), but considering the significant variations in solar wind temperature observed by Voyager 2 (Richardson et al. 2008), it falls within a realistic range. The ion-to-electron mass ratio is $m_i/m_e = 100$ for both the SWIs and PUIs, the ratio of upstream electron plasma frequency to cyclotron frequency is $\omega_{pe}/\Omega_e = 4$, and the relative PUI density is 25%. In the following, the run with $\Theta_{Bn} = 50°$ is mainly discussed. Hereafter, time is normalized to Ω_i^{-1}, velocity to v_A, and distance to v_A/Ω_i.

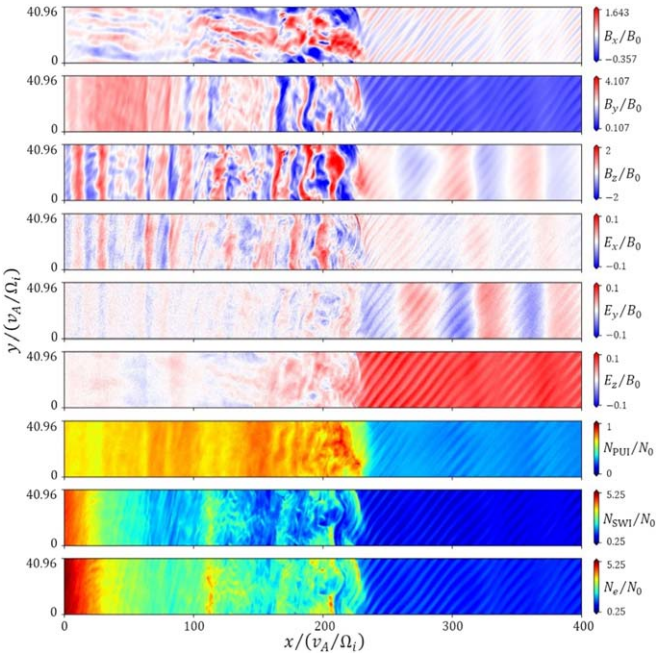

Figure 1. Structure of a PUI-mediated oblique shock at $t = 125$ ($\Theta_{Bn} = 50°$). From the top, the first three panels denote magnetic field B_x, B_y, B_z; the next three denote electric field E_x, E_y, E_z; and the last three indicate density of PUIs (N_{PUI}), SWIs (N_{SWI}), and electrons (N_e).

2.2. Overview

Figure 1 shows the structure of a shock at $t = 125$, where a shock ramp is at $x \sim 210$. The first three panels represent magnetic field B_x, B_y, B_z; the next three represent electric field E_x, E_y, E_z; and the last three indicate density of PUIs (N_{PUI}), SWIs (N_{SWI}), and electrons (N_e). Both upstream and downstream large-amplitude waves are generated.

Liu et al. (2010) showed, by performing a 2D hybrid simulation of a perpendicular shock including 20% PUIs, that Alfvén ion cyclotron (AIC) instability and mirror instability lead to the downstream turbulent field. The AIC waves are visible in B_x and B_z and mainly propagate along the downstream magnetic

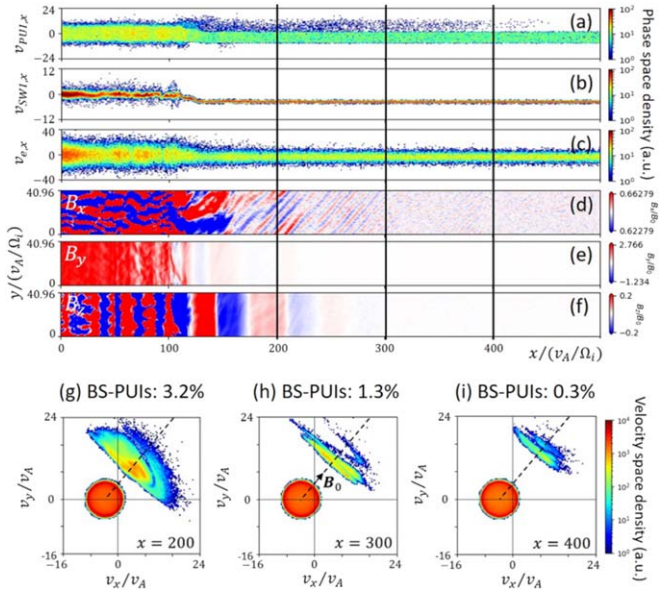

Figure 2. Particle distribution and magnetic fields upstream of the shock at $t = 65$ ($\Theta_{Bn} = 50°$). From the top, $V_x - x$ phase-space distributions of (a) PUIs, (b) SWIs, (c) electrons; magnetic field components of (d) B_x, (e) B_y, (f) B_z; and velocity distributions of PUIs at (g) $x = 200$, (h) $x = 300$, and (i) $x = 400$. In panels (a)–(c) and (g)–(i), only the particles at $y \approx L_y/2$ are counted. The color bars in panels (a)–(c) denote phase-space density (in an arbitrary unit). The color bar in panels (g)–(i) denotes velocity space density (in an arbitrary unit). The dashed lines in panels (g)–(i) represent the direction of local (upstream) magnetic field, B_0.

field, while the mirror waves have wavenumbers oblique to it and are the most visible in B_y. In Figure 1, however, the AIC wave signature is confirmed only in B_x. The signature of mirror waves in B_y and that of AIC waves in B_z are overwhelmed by the vertical stripes that are also seen in E_x and E_y.

The upstream waves are dominated by two types: relatively long wavelength waves propagating in the negative x-direction (vertical stripes), and relatively short wavelength waves propagating almost perpendicular to the ambient magnetic field (oblique stripes). These waves are convected by the upstream flow. The former are not only the origin of the downstream vertical structures discussed above but also the cause of shock surface reformation. We will discuss the generation mechanism of the upstream waves below.

2.3. Upstream Waves

In Figure 2 the $V_x - x$ phase-space distributions of (a) PUIs, (b) SWIs, and (c) electrons, whose positions in y are $y \approx L_y/2$, are shown, the corresponding magnetic field structures are represented in panels (d)–(f), and velocity space distributions of the PUIs at different positions in x are indicated in panels (g)–(i), respectively, at $t = 65$. The color scales in panels (a)–(c) and in panels (g)–(i) are in an arbitrary unit, and the color scale of the magnetic field is adjusted to appropriately see the upstream structures. It is clearly seen in panel (a) that some PUIs are reflected and backstreaming from the shock front at $x \approx 105$ toward upstream. On the other hand, as in the previous kinetic simulations of PUI-mediated shocks (Wu et al. 2009; Matsukiyo & Scholer 2014), no SWIs are reflected (panel (b)). This implies that the upstream waves are generated by these backstreaming PUIs (BS-PUIs). In the local velocity space at (g) $x = 200$, (h) $x = 300$, and (i) $x = 400$, the red circular populations denote incoming PUIs, while the BS-PUIs are

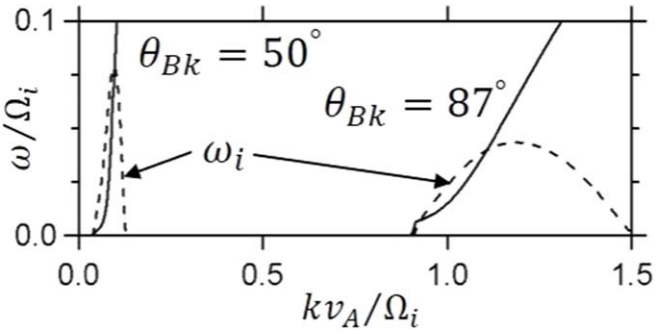

Figure 3. Linear dispersion relation of oblique resonant instability driven by BS-PUIs.

indicated by the rest in each panel. The BS-PUIs are well separated in the velocity space from the incoming PUIs, and their average velocities roughly align to the black dashed lines, indicating the direction of upstream magnetic field. The relative density of the BS-PUIs is 0.3% at $x = 400$, 1.3% at $x = 300$, and 3.2% at $x = 200$.

Since the BS-PUIs are regarded as a field-aligned beam, linear dispersion analysis of a beam-plasma system including background ions, electrons, and beam ions is performed. The details of the analysis are provided in the Appendix. In Figure 3 two unstable solutions obtained by solving the linearized Vlasov–Maxwell equation system are depicted. One is for $\theta_{Bk} = 50°$, and another is for $\theta_{Bk} = 87°$, where θ_{Bk} is the wave propagation angle with respect to the ambient magnetic field. For each solution, the solid line denotes the real part of frequency, while the dashed line shows the imaginary part. For $\theta_{Bk} = 50°$, the maximum growth rate occurs at $k \approx 0.096$. This corresponds to the relatively long wavelength waves having a wavenumber along the x-axis seen in Figures 2(e)–(f). The maximum growth rate occurs at $k \approx 1.2$ for $\theta_{Bk} = 87°$, which corresponds to the relatively short wavelength waves seen in Figure 2(d). These instabilities are interpreted as a resonant instability with oblique propagation angle.

2.4. Injection of PUIs

Figure 4(a) shows downstream energy distribution functions of ions at different times, $t = 75$ (orange), 100 (magenta), and 125 (red), where the energy is measured in the shock rest frame and normalized to the upstream bulk flow energy. Each solid line, indicating the distribution of whole ions, is divided into the two dashed lines with relatively low and high energy. The low- and high-energy ones denote SWIs and PUIs, respectively. It is evident that the high-energy tail of the PUIs evolves in time, indicating that the system has not reached a steady evolution state with a constant power-law index.

For comparison, simulations for $\Theta_{Bn} = 70°$ and $\Theta_{Bn} = 60°$ were additionally performed. At $\Theta_{Bn} = 70°$, no backstreaming ions were observed, and the downstream energy distribution remained steady during the same time interval, with no discernible accelerated component of PUIs. The energy distribution at this time ($t = 125$) is shown by the gray line. At $\Theta_{Bn} = 60°$, a very small amount of backstreaming ions was observed. As indicated by blue and cyan lines in Figure 4(a), the generation of accelerated PUIs can be observed over time, but the generation efficiency is evidently lower than that at $\Theta_{Bn} = 50°$. The energy densities of accelerated particles at $t = 125$, relative to the steady downstream plasma energy

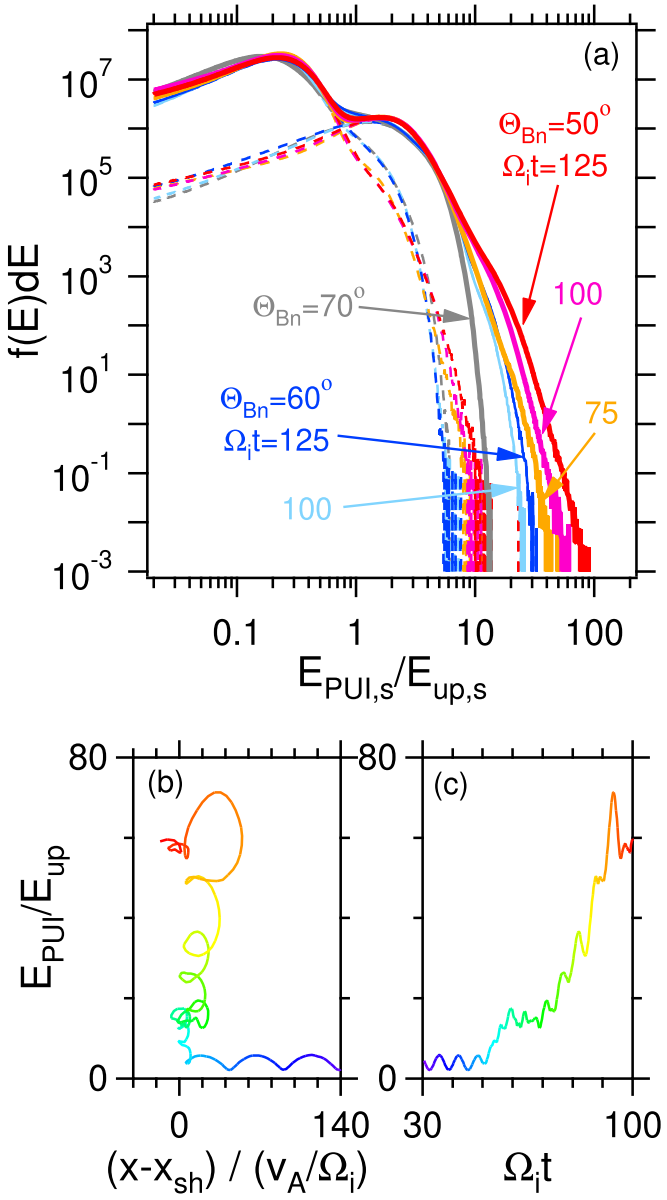

Figure 4. (a) Energy distributions of downstream PUIs at various shock angles and times. Each distribution (solid line) is divided into the two dashed lines indicating SWIs (lower energy) and PUIs (higher energy). Energy history of an accelerated PUI is shown by the rainbow colored lines as a function of (b) space and (c) time. The line color denotes time.

density at $\Theta_{Bn} = 70°$, are 0.066 when $\Theta_{Bn} = 60°$ and 0.13 when $\Theta_{Bn} = 50°$. We consider the shock angle of 60° to be close to the critical angle where particle backstreaming begins. At $\Theta_{Bn} = 50°$, the excitation of large-amplitude upstream waves by backstreaming PUIs is believed to increase the efficiency of accelerated PUI generation as discussed below.

The flux at the shoulder of the accelerated PUIs is roughly two orders of magnitude lower than the peak flux of PUIs. This relative flux of the shoulder looks comparable to or even higher than that seen in the past hybrid simulation with higher M_A (Giacalone et al. 2021). To explore the potential reasons for this difference, attention is drawn to the initial behavior of the accelerated particles. Evolution of energy of an accelerated PUI is depicted by the rainbow colored lines in Figures 4(b) and (c) as a function of relative distance from the shock and time, respectively. Here x_{sh} is the shock position averaged in the

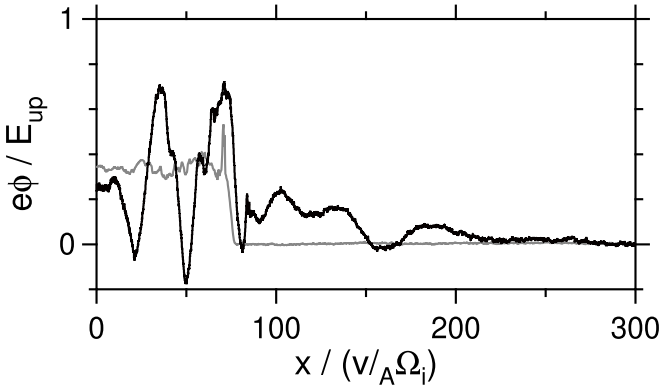

Figure 5. Electrostatic potential for $\Theta_{Bn} = 50°$ (black) and $\Theta_{Bn} = 70°$ (gray) at $t = 50$ along $y \approx 27$. The gray line is shifted horizontally in x to align the overshoot position with that of the black line.

y-direction, and the energy is measured in the simulation (downstream) frame. The PUI shows typical cycloidal motion up to $t \sim 50$. Once it is reflected, the PUI starts gaining energy. Beyond $t \sim 60$, there is an increase in energy accompanied by periodic fluctuations, indicative of shock drift acceleration (SDA) characteristics. In SDA, an ion gyrating across a shock has a relatively small gyroradius behind a ramp and a large gyroradius in front of it, so that the ion drifts along the shock surface parallel to the motional electric field. The small gyromotion behind a ramp is denoted in Figure 4(b) as the loop orbit. The same type of trajectory is reported by Giacalone & Decker (2010, see their Figure 3). However, upon careful observation of the trajectory, it is evident that there is another acceleration phase before $t \sim 60$, and the behavior of the particle during this phase differs from that observed afterward. When first reflected at $x \approx x_{sh}$, the particle exhibits a trajectory that is not looplike, indicating that the reflection occurs owing to potential. The subsequent second reflection is also similar, and such multiple reflections due to potential followed by incomplete gyromotion are characteristic of SSA.

Here the SSA can work because of the large-amplitude upstream waves. The black line in Figure 5 represents the profile of electrostatic potential normalized to upstream flow energy, $e\phi/E_{up}$, along $y \approx 27$ at $t = 50$, which is close to the time and position in y when the PUI in Figures 4(b) and (c) was first reflected at the shock. The fluctuation of potential is clearly seen both upstream and downstream of the shock ramp ($x \approx 80$). The upstream fluctuation is compressed and amplified at the shock. The potential occurs at about $0.2E_{up}$ at $x \approx 100$ already before the ramp. At the ramp, a large jump is seen, so that the potential reaches nearly $0.7E_{up}$. For comparison, the potential at $\Theta_{Bn} = 70°$ at the same time is indicated by the gray line. Here the x-value is shifted to align the overshoot position almost the same. Without backstreaming ions and upstream large-amplitude waves, both the foot by the reflected PUIs and steep ramp can be observed (although not clearly in this scale). The potential increase at the foot is about $0.3E_{up}$, and its spatial scale is approximately the gyroradius of the reflected PUIs, and the gradient of the potential in this part is smaller than that of the ramp at $\Theta_{Bn} = 50°$. The potential increase at the ramp is slightly over $0.2E_{up}$, and the total potential increase is smaller than that of $\Theta_{Bn} = 50°$. Note that the obliquely propagating waves contain an electrostatic field component. Therefore, the large-amplitude upstream waves accompany electrostatic potential. When $\Theta_{Bn} = 50°$, the waves are compressed at the

shock, so that the gradient of potential increases. The potential jump at the ramp occurs within a few ion inertial lengths, although it is larger than the electron inertial length that was originally assumed by Lee et al. (1996). Furthermore, the density increase due to the shock compression amplifies the potential. These effects can cause the observed SSA of the PUI, and this additional acceleration occurring immediately after the first reflection may enhance the production rate of the accelerated PUIs. Although we did not investigate all particles, we confirmed that, among the particles we examined, those with exceptionally high energy ($E_{\rm PUI}/E_{\rm up} > 60$ at $t = 100$) underwent the SSA process before the SDA process.

3. Summary

We investigated the injection process of PUI acceleration at a PUI-mediated oblique shock by using two-dimensional PIC simulation. The evolution of the system with sufficiently large spatial size in the shock normal direction was followed for a sufficiently long time ($t > 100$) to reproduce accelerated PUIs for the first time. Backstreaming PUIs drive large-amplitude waves through resonant instabilities. The convection of those large-amplitude waves causes shock surface reformation and alters the downstream structure. A part of PUIs are accelerated to tens of upstream flow energy with the timescale of $t \sim 100$ as observed in hybrid simulation by Giacalone et al. (2021). The initial acceleration occurs through the SSA mechanism followed by the SDA mechanism. The electrostatic potential accompanied by the large-amplitude upstream waves enables the SSA to occur.

McComas & Schwadron (2006) argue that low-energy particles are more likely to be accelerated at the terminal shocks in the flank of the heliosphere, where shock angles are oblique. The results discussed here qualitatively support this claim. However, the acceleration of particles in the tens of keV range discussed here requires shock angles of approximately 60° or less for injection, whereas typical shock angles at the flank may not be so small. It may be that the solar wind turbulence advocated by Giacalone & Decker (2010) and Giacalone et al. (2021) is necessary for injection.

Due to the finite system length in the y-direction, only limited wave modes are allowed to grow in our simulation. In the real system there should be other unstable wave modes with different θ_{Bk}. Those waves may lead to efficient scattering of the accelerated PUIs, which should be confirmed in the future. The accelerated particles in the tens of keV (∼tens of upstream flow energy) range observed at $\Theta_{Bn} = 50°$ correspond to the energy range of energetic neutral atoms targeted by the IMAP mission, and valuable insights into the particle injection site may be obtained from the data of its all-sky map.

Acknowledgments

We thank G. Zank, H. Washimi, and T. Hada for fruitful discussion. We also appreciate discussions at the team meeting "Energy Partition across Collisionless Shocks" supported by the International Space Science Institute in Bern, Switzerland. This research was supported by JSPS KAKENHI grant Nos. 19K03953, 22H01287, 23K22558 (S.M.), and 23K03407 (Y.M.). This work was supported by MEXT as "Program for Promoting Researches on the Supercomputer Fugaku" (Structure and Evolution of the Universe Unraveled by Fusion of Simulation and AI; grant No. JPMXP1020230406) and used computational resources of supercomputer Fugaku provided by the RIKEN Center for Computational Science (Project ID: hp230204, hp240219)

Appendix

The dispersion relations of upstream waves (Figure 3) are obtained by numerically solving the linearized Vlasov–Maxwell equation system. The detailed derivation of the dispersion equation including a beam component at oblique propagation is given in Chapter 8 of Gary (2005).

We assumed that there are three species, background ions, electrons, and beam ions. Each distribution function follows a (shifted-)Maxwellian distribution. The thermal velocity of electrons is 3.5, corresponding to an electron beta of 0.25. The electrons are given a drift velocity along the magnetic field to cancel out the current created by the beam ions. The background ions include both SWIs and PUIs, although we do not distinguish between the two and treat them as a single component of background ions at rest with an effective thermal velocity of 2.7. This value corresponds to an effective ion beta of 15, which is the sum of SWI beta and PUI beta. We will discuss the validity of this assumption later. As shown in Figure 2, the drift velocity of the beam ions varies depending on the distance from the shock. Here a representative value of 16 is used. The thermal velocity of beam ions is set to $v_{tb} = 1$. The beam population is actually propagating along the magnetic field with finite pitch angle so that the distribution function is a ring-beam type. This is the reason why the beam population in Figure 2(i) looks anisotropic in the velocity space. Since the ring velocity is clearly smaller than the beam velocity, we neglect the ring velocity in the dispersion analysis. Furthermore, a relative beam density of 0.3% is used. As long as the relative density is sufficiently small, the wavelength of the excited waves is hardly affected by it. The analysis is done in the frame of background ions.

Figure 3 is obtained with the above conditions. For $\theta_{Bk} = 50°$, the maximum growth rate occurs at $k \approx 0.096$ and $\omega \approx 0.07$. Since the argument of plasma dispersion function, $\zeta_b = (\omega - \mathbf{k}\cdot\mathbf{v_b} + \Omega_i)/\sqrt{2}\,k_{\parallel} v_{tb}$, is estimated as ≈0.95 (<1), the observed instability is a resonant instability. For $\theta_{Bk} = 87°$, the maximum growth rate occurs at $k \approx 1.2$ and $\omega \approx 0.065$, leading to $\zeta_b \approx 0.68$ (<1). Hence, the instability is also a resonant instability. Figure 6 shows the dependence of the dispersion relation on the beta of the background ions, β_i. For both $\theta_{Bk} = 50°$ and 87° cases, the maximum growth rate and the corresponding wavenumber do not change much, while β_i varies from 0.25 to 15. This indicates that our assumption of considering SWIs and incoming PUIs as a single background ion component was valid.

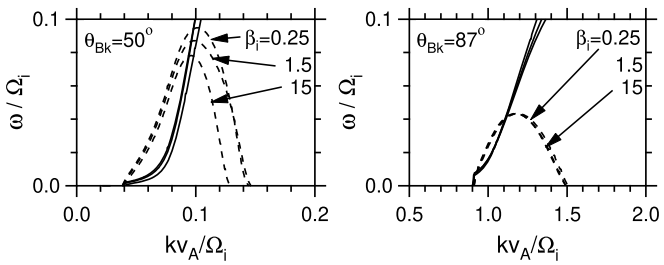

Figure 6. Linear dispersion relation of oblique resonant instability driven by BS-PUIs with different background ion beta, β_i. The solid and dashed lines indicate real and imaginary parts of frequency, respectively.

ORCID iDs

Shuichi Matsukiyo https://orcid.org/0000-0002-4784-0301
Yosuke Matsumoto https://orcid.org/0000-0002-1484-7056

References

Amano, T., Matsumoto, Y., Bohdan, A., et al. 2022, RvMPP, 6, 29
Balogh, A., & Treumann, R. A. 2013, Physics of Collsionless Shocks, ISSI Scientific Report Series, Vol. 12 (New York: Springer)
Blandford, R., & Eichler, D. 1987, PhR, 154, 1
Burgess, D., & Scholer, M. 2015, Collisionless Shocks in Space Plasmas, Cambridge Atmospheric and Space Science Series (Cambridge: Cambridge Univ. Press)
Chalov, S. 2006, in The Physics of the Heliospheric Boundaries, ISSI Scientific Report, Interstellar Pickup Ions and Injection Problem for Anomalous Cosmic Rays: Theoretical Aspect, 5, ed. V. Izmodenov & R. Kallenbach (Bern: International Space Science Institute), 245
Decker, R. B., Krimigis, S. M., Roelof, E. C., et al. 2008, Natur, 454, 67
Gary, S. P. 2005, Theory of Space Plasma Microinstabilities (Cambridge: Cambridge Univ. Press)
Giacalone, J., & Decker, R. 2010, ApJ, 710, 91
Giacalone, J., Nakanotani, M., Zank, G. P., et al. 2021, ApJ, 911, 27
Kumar, R., Zirnstein, E. J., & Spitkovsky, A. 2018, ApJ, 860, 156
Lee, M., Shapiro, V. D., & Sagdeev, R. Z. 1996, JGR, 101, 4777
Lee, R. E., Chapman, S. C., & Dendy, R. O. 2005, AnGeo, 23, 643
Lembege, B., & Yang, Z. 2016, ApJ, 827, 73
Lembege, B., & Yang, Z. 2018, ApJ, 860, 84
Lembege, B., Yang, Z., & Zank, G. P. 2020, ApJ, 890, 48
Li, H., Wang, C., & Richardson, J. D. 2008, GeoRL, 35, L19107
Liu, K., Gary, P., & Winske, D. 2010, JGRA, 115, A12114
Matsukiyo, S., & Scholer, M. 2011, JGRA, 116, A08106
Matsukiyo, S., & Scholer, M. 2014, JGRA, 119, 2388
Matsukiyo, S., Scholer, M., & Burgess, D. 2007, AnGeo, 25, 283
McComas, D. J., & Schwadron, N. A. 2006, GeoRL, 33, L04102
Nakanotani, M., Zank, G. P., & Zhao, L.-L. 2022, ApJ, 926, 109
Oka, M., Zank, G. P., Burrows, R. H., & Shinohara, I. 2011, AIP Conf. Proc. 1366, Energy Dissipation at the Termination Shock: 1D PIC Simulation (Melville, New York: AIP), 53
Pitňa, A., Šafránková, J., Němeček, Z., Ďurovcová, T., & Kis, A. 2021, FrP, 28, 626768
Richardson, J. D., Kasper, J. C., Wang, C., Belcher, J. W., & Lazarus, A. J. 2008, Natur, 454, 63
Stone, E. C., Cummings, A. C., McDonald, F. B., et al. 2005, Sci, 309, 2017
Swisdak, M., Giacalone, J., Drake, J. F., et al. 2023, ApJ, 959, 4
Trotta, D., Pecora, F., Settino, A., et al. 2022, ApJ, 933, 167
Trotta, D., Valentini, F., Burgess, D., & Servidio, S. 2021, PNAS, 118, e2026764118
Wang, B., Zank, G. P., Shrestha, B. L., et al. 2023, ApJ, 944, 198
Wu, P., Winske, D., Gary, S. P., Schwadron, N. A., & Lee, M. A. 2009, JGRA, 114, A08103
Yang, Z., Liu, Y. D., Richardson, J. D., et al. 2015, ApJ, 809, 28
Zank, G. P., Nakanotani, M., Zhao, L.-L., et al. 2021, ApJ, 913, 127
Zank, G. P., Pauls, H. L., Cairns, I. H., & Webb, G. M. 1996, JGR, 101, 457